# OPTICAL COHERENCE TOMOGRAPHY IMAGE SEGMENTATION

*Jinming Duan*[*], *Christopher Tench*[†], *Irene Gottlob*[‡], *Frank Proudlock*[‡], *Li Bai*[*]

[*]School of Computer Science, University of Nottingham, UK
[†]Medical School, University of Nottingham, UK
[‡]Ophthalmology Department, University of Leicester, UK

## ABSTRACT

Optical coherence tomography (OCT) is a three-dimensional non-invasive imaging technique that can generate images of the eye at microscopic level to help diagnosis of eye diseases. However, OCT images often suffer from inhomogeneity and are corrupted by speckle noise, posing challenges to automated OCT image segmentation and analysis. In this paper, a novel method is proposed to segment retinal layers in OCT images. The proposed method uses a coarse-to-fine approach to segmentation and includes: (1) A variational retinex model that can enhance the details as well as correct the intensity inhomogeneities; (2) An anisotropic coherent enhancing diffusion that can remove speckle noise and simultaneously connect the interrupted retinal layers; (3) A nonlinear isotropic filter that smooths the processed OCT image and leads to the initial coarse segmentation; (4) A high-pass unsharp masking filter that highlights the remaining layers and gives the fine segmentation. Afterwards, all the retinal layers that can be seen by human eyes are segmented accurately using common edge detection of region based segmentation algorithms. Extensive experiments results validate the effectiveness and performance of the proposed method.

***Index Terms***— Optical coherence tomography (OCT), variational retinex, nonlinear diffusion, unsharp masking, image segmentation

## 1. INTRODUCTION

In OCT imaging, intensity inhomogeneity may be caused by non-uniformity in the optical field during image acquisition [1], which poses significant challenges to intensity-based image segmentation methods. As OCT imaging technique is based on the detection of optical coherent waves, images produced usually contain a great amount of speckle noise [2]. The noise can degrade image quality and pose challenges for image segmentation algorithms. Furthermore, some retinal layer boundaries in the OCT image appear discontinuous due to shadows cast by blood vessels [3], as shown in Fig. 7 (a). This further makes automated image segmentation difficult.

In this paper, a novel method is introduced for segmenting retinal layers in the OCT image. The proposed approach employs a sequence of image enhancement procedures to overcome the problems with OCT images, leading to more accurate segmentation. Specifically, an improved variational retinex model using TV (total variation) regulariser [4] and its efficient fast split Bregman [5] is used first to correct intensity inhomogeneity and enhance the features in the image. This is followed by anisotropic coherent enhancing diffusion [6] to remove speckle noise and simultaneously connect the discontinuous retinal layer boundaries. A nonlinear isotropic diffusion [7] then simplifies the pre-processed image and enables the coarse level segmentation. A high-pass unsharp masking filter is then applied to sharpen the thin and low-contrast retinal layers for the fine level segmentation. All existing visible layers are successfully segmented using the region growing method for both coarse and fine segmentation. The proposed method is validated through experiments.

## 2. VARIATIONAL RETINEX MODEL

A TV (total variation) based retinex variational model and its fast algorithm are proposed to correct inhomogeneity in OCT images. The retinex problem is posed as

$$S = RL \tag{2.1}$$

where $S$ is observed image, $R$ is the reflectance (i.e. the enhancement image) whose intensity interval is [0,1], and $L$ is illumination. To model the inverse problem, the additive version is obtained by taking logarithm of both side of (2.1)

$$s = r + l \tag{2.2}$$

Since illumination $l$ is supposed to be smooth and reflectance $r$ contains sharp details (i.e. edges), we proposed following variational functional for image enhancement

$$E(r) = \alpha \int_\Omega r^2 + \int_\Omega |\nabla (s - r)|^2 + \beta \int_\Omega |\nabla r| \tag{2.3}$$

with constraint $r \leq 0$ to guarantee the intensities of reflectance $R$ lie in [0,1]. The first quadratic fidelity term on the right-hand side enforces the similarity between illumination and observed image. Theoretically, the penalty parameter

imposed on this term should be weak in order not to pull $l$ down too much towards $s$. The second term introduces $H^1$ smoothness prior on the illumination $l$. The third term uses TV regulariser weighted by a positive coefficient $\beta$ for the reflectance $r$, which is more effective than the $H^1$ regulariser used in Kimmel's work [8, 9].

To minimise $L^1$ based functional (2.3) effectively, the following split Bregman algorithm is designed by introducing an auxiliary vector $\boldsymbol{w}$ and a Bregman iterative parameter $\boldsymbol{b}$.

$$E(r, \boldsymbol{w}, \boldsymbol{b}) = \alpha \int_\Omega r^2 + \int_\Omega |\nabla s - \boldsymbol{w}|^2 + \beta \int_\Omega |\boldsymbol{w}| + \theta \int_\Omega |\boldsymbol{w} - \nabla r - \boldsymbol{b}|^2 \quad (2.4)$$

Equation (2.4) is a multivariate minimization problem usually solved by an optimization procedure. First $\boldsymbol{w}$ and $\boldsymbol{b}$ are fixed to optimise $r$ by employing the fast Fourier transform

$$r = \Re\left(\mathcal{F}^{-1}\left(\frac{\theta\mathcal{F}(div)\,\mathcal{F}(\boldsymbol{b} - \boldsymbol{w})}{\alpha - \theta\mathcal{F}(\Delta)}\right)\right)$$

where $\mathcal{F}$ and $\mathcal{F}^{-1}$ denotes the discrete Fourier transform and inverse Fourier transform respectively. $div$ and $\Delta$ are respectively divergence and Laplace operators. $\Re$ is the real part of a complex number. "$-$" stands for pointwise division of matrices. $r = min(r, 0)$ is then implemented to satisfy constraint $r \leq 0$.

$r$ is fixed next and the following analytical shrink is used to solve vector $\boldsymbol{w}$

$$\boldsymbol{w} = \max(|\boldsymbol{y}| - \beta, 0)\,\frac{\boldsymbol{y}}{(1+\theta)\,|\boldsymbol{y}|} \quad (2.5)$$

where $\boldsymbol{y} = \nabla s + \theta(\nabla r + b)$. Note that shrink (2.5) includes two subshrink for each component of vector $\boldsymbol{w}$.

Finally, Bregman iterative parameter $\boldsymbol{b}$ is solved by

$$\boldsymbol{b} = \boldsymbol{b} + \nabla r - \boldsymbol{w}$$

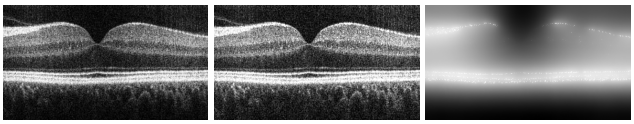

(a) (b) (c)

**Fig. 1**. Enhance and correct inhomogeneity in the original OCT image. (a) Original OCT image; (b) Enhanced and homogeneous image; (c) Estimated illumination from the first image.

## 3. NONLINEAR DIFFUSION

Two nonlinear filters (i.e. the anisotropic and isotropic) based on partial differential equations are used to further process the enhanced OCT image Fig. 1 (b).

### 3.1. Anisotropic diffusion

The layer boundaries in the OCT images are generally directional flow-like structures. It is possible to strengthen these structures mathematically, using anisotropic CED (coherence enhancing diffusion).

$$\partial_t u = div\left(\boldsymbol{D}(\boldsymbol{J}_p)\,\nabla u\right) \quad (3.1)$$

where $\partial_t u$ denotes the first derivative with regards to diffusion time $t$, and $\boldsymbol{J}_p$ is the smoothed version of the structure tensor $\boldsymbol{J}$ by using a Gaussian kernel with standard deviation $p$

$$\boldsymbol{J}_p = K_p * \boldsymbol{J} = \begin{pmatrix} j_{11}, j_{12} \\ j_{21}, j_{22} \end{pmatrix} \quad (3.2)$$

Structure tensor $\boldsymbol{J}$ is defined as

$$\boldsymbol{J} = \nabla u_\sigma \nabla u_\sigma^{\mathrm{T}} = \begin{pmatrix} u_{x\sigma}^2,\ u_{x\sigma}u_{y\sigma} \\ u_{y\sigma}u_{x\sigma}, u_{y\sigma}^2 \end{pmatrix}$$

where $\nabla u_\sigma = K_\sigma * \nabla u = K_\sigma * (u_x, u_y)^{\mathrm{T}}$, the smoothed version of the gradient convoluted by a Gaussian Kernel $K_\sigma$. The standard deviation $\sigma$ controls the size of the resulting flow-like patterns. Increasing $\sigma$ leads to an increased distance between the resulting flow lines.

The parameter $p$ averages orientation information and helps to stabilise the directional behaviour of the diffusion and connect interrupted lines if $p$ is equal or larger than the gap size. The convolution with the Gaussian kernels $K_\sigma$ and $K_p$ makes the structure tensor measure more coherent.

To solve Equation (3.1), $\boldsymbol{J}_p$ is rewritten in terms of its eigenvalues and eigenvectors as follows

$$\boldsymbol{J}_p = \mu_1 \boldsymbol{v_1} \boldsymbol{v_1}^{\mathrm{T}} + \mu_2 \boldsymbol{v_2} \boldsymbol{v_2}^{\mathrm{T}} \quad (3.3)$$

where eigenvalues of $\boldsymbol{J}_p$ are

$$\mu_{1,2} = \frac{1}{2}\left(j_{11} + j_{22} \pm \sqrt{(j_{11} - j_{22})^2 + 4j_{12}^2}\right) \quad (3.4)$$

where we assign $\mu_1 > \mu_2$. The two normalised eigenvectors of the structure tensor $\boldsymbol{J}_p$ are $\boldsymbol{v_1} = (cos\theta, sin\theta)^{\mathrm{T}}$ and $\boldsymbol{v_2} = (-sin\theta, cos\theta)^{\mathrm{T}}$. It is easy to check that

$$\begin{cases} j_{11} = \mu_1 \cos^2\theta + \mu_2 \sin^2\theta \\ j_{12} = (\mu_1 - \mu_2)\sin\theta\cos\theta \\ j_{22} = \mu_1 \sin^2\theta + \mu_2 \cos^2\theta \end{cases} \quad (3.5)$$

$\boldsymbol{D}(\boldsymbol{J}_p)$ in Equation (3.1) is the diffusion tensor that is positive definite symmetric $2 \times 2$ matrix, and is defined as

$$\boldsymbol{D}(\boldsymbol{J}_p) = \begin{pmatrix} d_{11}, d_{12} \\ d_{21}, d_{22} \end{pmatrix} = \lambda_1 \boldsymbol{v_1} \boldsymbol{v_1}^{\mathrm{T}} + \lambda_2 \boldsymbol{v_2} \boldsymbol{v_2}^{\mathrm{T}} \quad (3.6)$$

This tensor has two orthonormal eigenvectors $\boldsymbol{v_1}$ and $\boldsymbol{v_2}$ as the smoothed structure tensor $\boldsymbol{J}_p$ in (3.2) and uses two diffusivities $\lambda_1$ and $\lambda_2$ to control the diffusion speed in two di-

rections (i.e. parallel and perpendicular to the gradient direction). The details of $\lambda_1$ and $\lambda_2$ read

$$\lambda_1 = \gamma$$
$$\lambda_2 = \begin{cases} \gamma & \mu_1 = \mu_2 \\ \gamma + (1-\gamma)\exp\left(\frac{-C}{(\mu_1-\mu_2)^2}\right) & \text{else} \end{cases} \quad (3.7)$$

where $\gamma$ is a small positive value to keep $\boldsymbol{D}$ positive definite and $C$ is the coherence parameter. According to (3.4), (3.5), and (3.6). The components in the diffusion tensor $\boldsymbol{D}(\boldsymbol{J}_p)$ are deduced as

$$\begin{cases} d_{11} = \frac{\lambda_1+\lambda_2+(\lambda_1-\lambda_2)(j_{11}-j_{22})/(\mu_1-\mu_2)}{2} \\ d_{12} = \frac{j_{12}(\lambda_1-\lambda_2)}{(\mu_1-\mu_2)} \\ d_{22} = \frac{\lambda_1+\lambda_2-(\lambda_1-\lambda_2)(j_{11}-j_{22})/(\mu_1-\mu_2)}{2} \end{cases}$$

Equation (3.1) can now be evolved by setting an artificial time step $t$. However, due to CFL condition, $t$ must be small enough (i.e. $t < 0.25$) to ensure convergence. Fortunately, the semi-implicit AOS (additive operator splitting) scheme can be used to improve the stability and accelerate the convergence.

(a) (b) (c)

**Fig. 2**. First (i.e. main layers) segmentation. (a) Despeckled result of Fig. 1 (b) by CED method; (b) Diffused result of (a) by the isotropic diffusion (3.8); (c) Segmentation result of (b) via region grow.

### 3.2. Isotropic diffusion

Fig. 2 shows the diffusion result by the anisotropic CED method on the enhanced image in Fig. 1. Note that the speckle noise is efficiently removed and the flow-like features are well enhanced. For comparison, several known models are tried to directly segment Fig. 2 (a), including snake model [10], geodesic active contour model [11], Chan-vese model [12, 13] and Mumford-Shah model [14]. The results of these methods shown in Fig. 6 are not satisfactory. The reasons for the failure are (1) the methods are sensitive to parameters and to the initial contour; (2) edges in the diffused image are blurred due to the twice use of Gaussian convolution in the CED method; (3) the OCT image have several layers, some of which hold similar gray value; (4) some layers are of low-contrast. In fact, it is difficult to segment all the layers simultaneously by using only one method. Thus, we divide the segmentation process into two stages. In the first stage, an isotropic filter introduced is used to remove these layers that are thin and low-contrast from Fig. 2 (a) and obtain the main/thick layers shown in Fig. 2 (b). The main/thick layers after the diffusion can be easily segmented into several different regions using a simple region growing method, which is shown in Fig. 2 (c). In the second stage, an unsharp masking filter is used on the image diffused by CED method to sharpen the thin and low-contrast layers before segmentation using region growing. All the visible layers can be segmented after the two stages.

In [7], Perona and Malik proposed the following isotropic diffusion

$$\partial_t u = div\left(g\left(|\nabla u_\sigma|\right)\nabla u\right) \quad (3.8)$$

where $g\left(|\nabla u_\sigma|\right)$ is a non-increasing diffusivity, different from the structure tensor used in (3.1) in last section. Function $g$ allows isotropic diffusion in flat regions and no diffusion near the edges. It is defined as

$$g(s) = 1 - \exp\left(\frac{-C_m}{(s/\lambda)^m}\right) \quad (3.9)$$

The constant $C_m$ is automatically calculated in such way that $(\partial\Phi(s)/\partial s)|_{s=\lambda} = 0$, where $\Phi(s) = sg(s)$. Parameter $m$ determines how fast the diffusivity $g$ changes, and $\lambda$ controls smoothness of the diffused image. The AOS scheme is then applied to solve (3.8). Fig. 2 (b) shows the diffusion result by this method.

## 4. UNSHARP MASKING

Unsharp masking is a flexible and powerful way to increase sharpness, and it can greatly enhance the appearance of fine details by increasing small-scale acutance. Thus, it will be suitable for boosting the faint and thin layers in the OCT image, making the second fine segmentation possible. The definition of the unsharp masking is

$$g = f + k\left(f - G_\sigma * f\right) \quad (4.1)$$

where $f$ is blurred input image, an $k$ is a positive parameter. Greater $k$ means high-boost emphasis of high frequencies (i.e. edges). $G_\sigma$ is Gaussian kernel with standard deviation $\sigma$. Fig. 3 illustrates the mechanics of the high-pass filter.

In Fig. 4, we test different parameters in (4.1) to sharpen Fig. 2 (a). It can be seen that as the $k$ increases, these blurred and thin layers become more obvious. The region growing method is then applied to the remaining thin retinal layers in Fig. 4 (b) which were not segmented in the first stage. After this stage, we can obtain all the existing layers in the original OCT image Fig. 1 (a). The second segmentation and final results are demonstrated in the following Fig. 5.


(a) (b) (c) (d)

**Fig. 3**. 1D illustration of the mechanics of unsharp masking. (a): Original signal; (b) Blurred signal using Gaussian filter, with original shown dasked for reference; (c) Unsharp masking (i.e. subtract the blurred version from the original); (d): Sharpened signal obtained by adding (c) to (a).

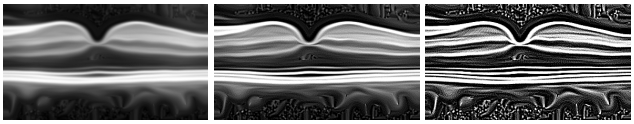

(a) $\sigma = 1, k = 5$ (b) $\sigma = 1, k = 10$ (c) $\sigma = 1, k = 50$

**Fig. 4**. Sharpen the blurred and thin layers in Fig. 2 (a) using different parameters in equation (4.1).

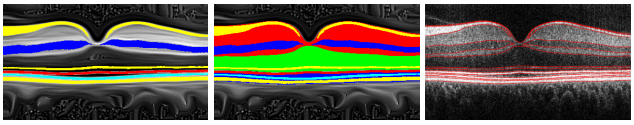

(a) (b) (c)

**Fig. 5**. Second segmentation and final results. (a): The second segmentation result of Fig. 4 (b) via region growing; (b) Combined result of first and second segmentations; (c): Final segmentation result in red.

## 5. EXPERIMENTAL RESULTS

Several experiments on various OCT images are presented to illustrate the effectiveness and performance of the proposed OCT segmentation method.

In Fig. 6, we present segmentation results of several methods on the despeckled image Fig. 2 (a) which is easier to segment than the original image. It is clear that these methods are not able to extract all the retinal layers in the OCT image.

In Fig. 7, we demonstrate that the proposed method can successfully segment the OCT image that contains some broken retinal layers (indicated by red arrows). Some layers in Fig. 7 (a) are interrupted due to the shadow effect. They are connected using anisotropic diffusion (3.1) as shown in Fig. 7 (d). These layers are then highlighted after applying the unsharp masking filter, as shown in Fig. 7 (f). This leads to the second fine segmentation presented in Fig. 7 (h). In addition, One can see in Fig. 7 (e) the isotropic diffusion can greatly simplify the complex OCT image and thus provide the first coarse segmentation result in Fig. 7 (g). All the visible retinal layers can be elegantly extracted after combining the two segmentation. The result is shown in the last image Fig. 7 (i).

The last experiment in Fig. 8 further illustrate the effectiveness of the proposed method. Note that these existing retinal layers including these thin and low-contrast ones can be correctly extracted by the proposed method.

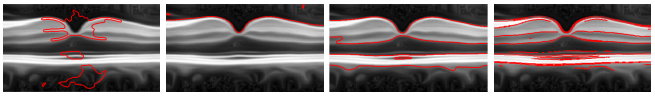

**Fig. 6**. Segmentation results of different methods. From left to right are results by snake model [10], geodesic active contour model [11], Chan-vese model [12, 13] and Mumford-Shah model [14], respectively.

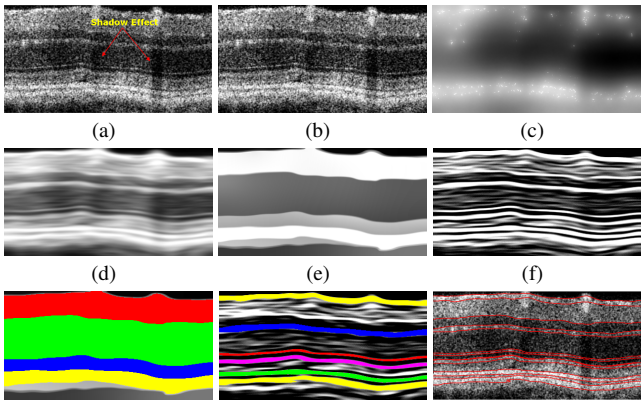


(a) (b) (c)

(d) (e) (f)

(g) (h) (i)

**Fig. 7**. Segmentation of OCT image with broken retinal layers. (a) Original image; (b) Enhanced image by TV retinex model; (c) Estimated illumination from (a); (d) Despeckled result of (b) using anisotropic CED method; (e) Diffused result of (d) by the isotropic diffusion (3.8); (g)-(h) Segmentation results by region growing based on (e) and (f); (i): Final segmentation result shown in red.

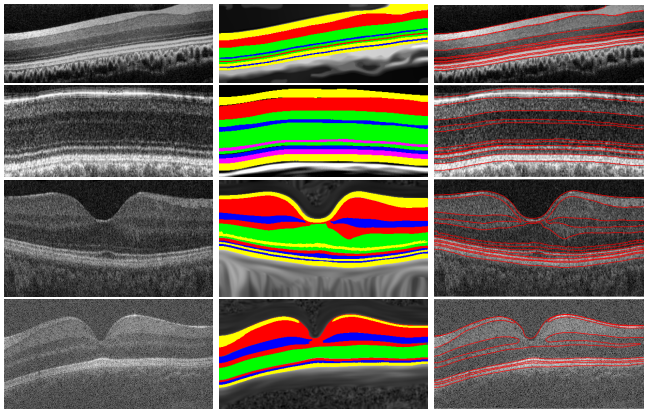

**Fig. 8**. Segmentation results. 1st column: Original images; 2nd column: Combined the two segmentation results with different colors drawn on different retinal layers; 3rd column: Final results shown in reds.

## 6. CONCLUSION

In this paper, a novel method is presented for segmenting retinal layers in OCT images. The proposed approach corrects intensity inhomogeneity, removes speckle noise, connects interrupted/discontinuous layer boundaries, as well as enhances/sharpens weak image features (i.e. thin layers), thus allowing effective retinal layer segmentation with a simple region growing method. Experimental results show that the proposed method is capable of segmenting all the retinal layers that can be seen by human eyes. Future work will involve expending the method to 3D and further developing OCT image analysis tools based on variational methods [15–17] for ophthalmologists.

## 7. REFERENCES


[1] Marjan Razani, Timothy WH Luk, Adrian Mariampillai, Peter Siegler, Tim-Rasmus Kiehl, Michael C Kolios, and Victor XD Yang, "Optical coherence tomography detection of shear wave propagation in inhomogeneous tissue equivalent phantoms and ex-vivo carotid artery samples," *Biomedical optics express*, vol. 5, no. 3, pp. 895–906, 2014.

[2] Prabakar Puvanathasan and Kostadinka Bizheva, "Speckle noise reduction algorithm for optical coherence tomography based on interval type ii fuzzy set," *Optics express*, vol. 15, no. 24, pp. 15747–15758, 2007.

[3] Michaël JA Girard, Nicholas G Strouthidis, C Ross Ethier, and Jean Martial Mari, "Shadow removal and contrast enhancement in optical coherence tomography images of the human optic nerve head," *Investigative ophthalmology & visual science*, vol. 52, no. 10, pp. 7738–7748, 2011.

[4] Leonid I Rudin, Stanley Osher, and Emad Fatemi, "Nonlinear total variation based noise removal algorithms," *Physica D: Nonlinear Phenomena*, vol. 60, no. 1, pp. 259–268, 1992.

[5] Tom Goldstein and Stanley Osher, "The split bregman method for l1-regularized problems," *SIAM Journal on Imaging Sciences*, vol. 2, no. 2, pp. 323–343, 2009.

[6] Joachim Weickert, *Anisotropic diffusion in image processing*, vol. 1, Teubner Stuttgart, 1998.

[7] Pietro Perona and Jitendra Malik, "Scale-space and edge detection using anisotropic diffusion," *Pattern Analysis and Machine Intelligence, IEEE Transactions on*, vol. 12, no. 7, pp. 629–639, 1990.

[8] Ron Kimmel, Michael Elad, Doron Shaked, Renato Keshet, and Irwin Sobel, "A variational framework for retinex," *International Journal of computer vision*, vol. 52, no. 1, pp. 7–23, 2003.

[9] Yuanyuan Zang, Zhenkuan Pan, Jinming Duan, Guodong Wang, and Weibo Wei, "A double total variation regularized model of retinex theory based on nonlocal differential operators," in *Image and Signal Processing (CISP), 2013 6th International Congress on*. IEEE, 2013, vol. 1, pp. 213–218.

[10] Michael Kass, Andrew Witkin, and Demetri Terzopoulos, "Snakes: Active contour models," *International journal of computer vision*, vol. 1, no. 4, pp. 321–331, 1988.

[11] Vicent Caselles, Ron Kimmel, and Guillermo Sapiro, "Geodesic active contours," *International journal of computer vision*, vol. 22, no. 1, pp. 61–79, 1997.

[12] Tony F Chan and Luminita A Vese, "Active contours without edges," *Image processing, IEEE transactions on*, vol. 10, no. 2, pp. 266–277, 2001.

[13] Jinming Duan, Zhenkuan Pan, Xiangfeng Yin, Weibo Wei, and Guodong Wang, "Some fast projection methods based on chan-vese model for image segmentation," *EURASIP Journal on Image and Video Processing*, vol. 2014, no. 1, pp. 1–16, 2014.

[14] Jianhong Shen, "$\gamma$-convergence approximation to piecewise constant mumford-shah segmentation," in *Advanced Concepts for Intelligent Vision Systems*. Springer, 2005, pp. 499–506.

[15] Y Ding, WOC Ward, T Wästerlid, PA Gowland, AM Peters, J Yang, and L Bai, "Three-dimensional vessel segmentation using a novel combinatory filter framework," *Physics in medicine and biology*, vol. 59, no. 22, pp. 7013, 2014.

[16] Jinming Duan, Wenqi Lu, Guodong Wang, Zhenkuan Pan, and Li Bai, "Second order model for image decomposition using the split bregman algorithm," in *International Conference on Intelligence Science and Big Data Engineering*. Springer, 2015.

[17] Jinming Duan, Yuchun Ding, Zhenkuan Pan, Jie Yang, and Li Bai, "Second order mumford-shah model for image denoisingl," in *International conference on image processing*. IEEE, 2015.